Drag Force on a Starting Plate Scales with the Square Root of Acceleration

J. Reijtenbagh, * M. J. Tummers, and J. Westerweel
Laboratory for Aero and Hydrodynamics, Delft University of Technology, Mekelweg 2, 2628 CD Delft, Netherlands

(Received 18 November 2022; accepted 24 March 2023; published 24 April 2023)

We report results on the instantaneous drag force on plates that are accelerated in a direction normal to the plate surface, which show that this force scales with the square root of the acceleration. This is associated with the generation and advection of vorticity at the plate surface. A new scaling law is presented for the drag force on accelerating plates, based on the history force for unsteady flow. This scaling avoids previous inconsistencies in using added mass forces in the description of forces on accelerating plates.

DOI: 10.1103/PhysRevLett.130.174001

An object that is moving through a fluid is generally studied for the case of a steady or quasisteady velocity. However, in reality all objects must have started from rest before reaching their target velocity. Also, objects in a practical situation rarely move at an exact stationary velocity, and in certain situations the motion can be strongly instationary; for example, in biological propulsion [1–3], flight applications [4–6], or the motion of a rowing blade [7].

We consider the drag force acting on a normal flat plate as a function of the acceleration until it reaches a target velocity. The conventional approach is to describe the forces on an accelerating, or decelerating, plate at high Reynolds number ($\mathrm{Re} \gg 1$) by considering the added mass force combined with a quasisteady drag force, where the added mass force is directly proportional to the acceleration [8–10]. The inviscid nature of added mass is a reason for doubting this approach [11–13] and recent experiments [7,14,15] demonstrate that this description is incomplete, and the dependence of the drag force on acceleration, velocity, and other parameters has not been described by a general scaling law.

In this Letter we present experimental findings on the drag force of accelerating normal plates in a viscous fluid at high Reynolds numbers. From these experimental data we find a novel scaling law for the drag force on accelerating plates. This scaling law states that the peak drag force is proportional to the square root of the (constant) acceleration, which shows that a constant added mass does not accurately predict the measured drag and an alternative contribution to the drag force due to acceleration needs to be considered.

In our experiments we measure the drag force on a circular disk, a square plate, and a 1:2 aspect ratio rectangular plate, all with a frontal area $A = 0.020\ \mathrm{m}^2$, that are uniformly accelerated from rest at various rates to given target velocities. The experiments were carried out in a $2.0 \times 2.0 \times 0.5\ \mathrm{m}^3$ water-filled tank, where an industrial gantry robot was used to accelerate the plates. The acceleration a in the experiments ranges from 0.10 to $1.64\ \mathrm{m/s}^2$ with target velocities V_a ranging from 0.30 to 1.20 m/s, which corresponds to a Reynolds number range from 30×10^3 to 120×10^3. A six-axis force-torque transducer is used to measure the force $F(t)$ on the plate. Planar particle image velocimetry (PIV) measurements were done to measure the instantaneous vorticity field and circulation. A schematic of the experiment can be found in Fig. 1(a); further details can be found in Ref. [7].

Given the measured total force $F(t)$, the drag force F_D on an accelerating plate with mass m submerged in a fluid with density ρ and kinematic viscosity ν, at high Reynolds number ($\mathrm{Re} \gg 1$), can be written as [8,15]

$$F_D(t) \equiv F(t) - ma(t) = \underbrace{C_D \frac{1}{2}\rho V^2(t) A}_{F_{\mathrm{QS}}(t)} + F_a(t), \quad (1)$$

where C_D is the drag coefficient, A is the frontal area of the plate, $V(t)$ is the instantaneous velocity of the plate, and $a(t) \equiv \dot{V}(t)$ is the acceleration. The first term on the right-hand side is the quasisteady drag force $F_{\mathrm{QS}}(t)$. This term represents the form drag, proportional to the stagnation pressure $\frac{1}{2}\rho V^2$, with a proportionality constant C_D that is (nearly) constant over a large range in Reynolds number for a thin flat plate [9,16]; the second term, $F_a(t)$, is a hydrodynamic force due to the acceleration.

A contemporary interpretation of Eq. (1) would separate the drag force for an accelerating plate into circulatory and noncirculatory contributions [17,18], where the noncirculatory contribution is equal to the conventional added mass [9]. This approach requires measured velocity data, and as such is not able to provide an *a priori* scaling for the drag force with acceleration.

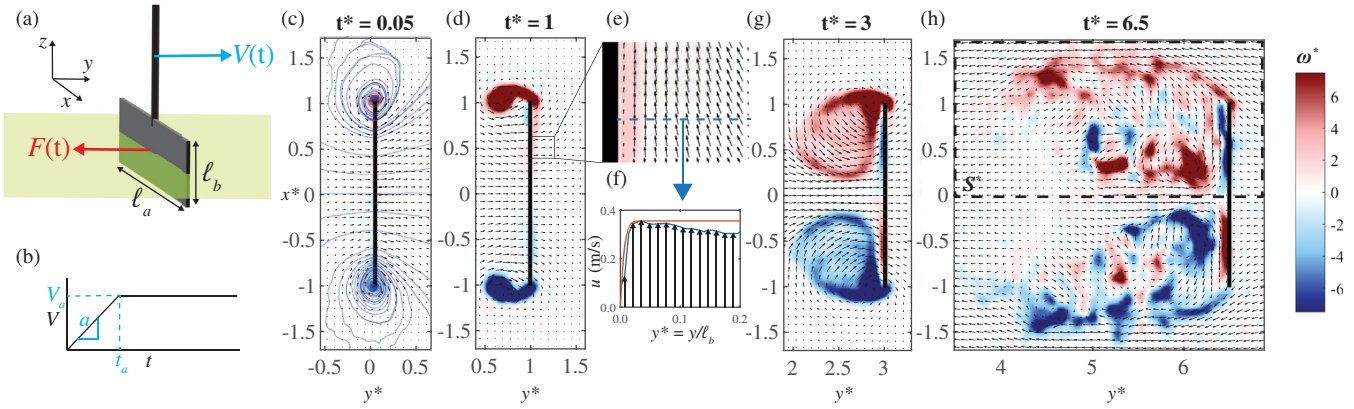

FIG. 1. (a) A plate with dimensions $\ell_a \times \ell_b$ moves through a viscous fluid at velocity $V(t)$ and experiences a force $F(t)$. PIV measurement plane (green) at the plate midplane. (b) Imposed velocity $V(t)$ of the plate: $V = at$ (with constant acceleration a) for $0 < t < t_a$ and constant V_a for $t > t_a$. (c),(d),(g),(h) Measured velocity fields and vorticity ω^* for $a^* = 0.5$ ($t_a^* = 1.0$) at $t^* = 0.05$ (with streamlines), 1.0, 3.0, 6.5, respectively. (e) Detail near upstream plate surface. (f) Velocity profile along blue dashed line in (e); red line represents the velocity profile according to Eq. (4). The plate velocity is subtracted for (e) and (h). All dimensions are normalized by ℓ_b.

$F_a(t)$ is usually considered as a (noncirculatory) added mass force [$= m_v a(t)$] that follows from potential flow theory [9], with a constant "virtual mass" m_v [19] of fluid that is accelerated with the object. The value of m_v depends on the object shape and direction of motion [10,20]. The ratio of the added mass force and quasisteady drag force defines the dimensionless acceleration $a^* = a\ell/V_a^2$ [14,15,21,22], which has previously been used in attempts to scale drag forces for accelerating objects. Furthermore, we present results as a function of the dimensionless time t^*, defined as [23,24]

$$t^* = \frac{1}{\ell}\int_0^t V(\tau)d\tau, \tag{2}$$

where ℓ is a reference length scale; here the plate height ℓ_b, so that t^* is equal to the number of plate heights traveled. The dimensionless duration of the acceleration t_a^* is equal to $(2a^*)^{-1}$.

Figure 1 shows the flow field in the midplane of the rectangular plate. The flow pattern initially resembles the flow field given by potential flow theory, but due to the no-slip condition at the plate surface and finite fluid viscosity, vorticity is generated near the plate edges [Fig. 1(c)] and plate surface, and forms a thin boundary layer [Figs. 1(d)–1(f)] resembling Hiemenz flow [25]. This vorticity is advected into the vortex that forms near the edges of the plate, and increases its circulation Γ. During the acceleration the vortex near the plate edges grows over time and the flow field diverges from the initial potential flow field; see Fig. 1(d). This is a first indication that conventional (noncirculatory) added mass, which originates from potential flow, is insufficient to explain the forces that occur due to acceleration. Around $t^* \cong 6$, the initial vortex near the plate edge breaks up, detaches from the plate, and a turbulent three-dimensional wake develops; see Fig. 1(h). We refer the reader to the video in the Supplemental Material to see the development of the flow around the accelerating plate [26].

Figure 2 shows the measured drag force F_D on a 100×200 mm^2 rectangular plate for accelerations between 0.10 and 1.64 m/s^2 toward the same target velocity V_a [$= at_a$; see Fig. 1(b)] of 0.45 m/s as a function of t^*. Toward the highest acceleration only accelerations that increase with a factor 2 are shown for clarity. After the acceleration ends, all lines collapse on a single curve for sufficiently large values of t^*. The circles indicate the peak

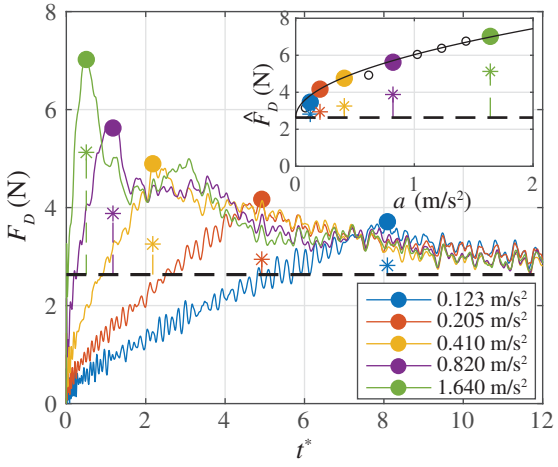

FIG. 2. Measured drag force F_D for different accelerations toward velocity $V_a = 0.45$ m/s. Full circles indicate the end of the acceleration. The black dashed line indicates the steady state drag ($F_{QS} = \frac{1}{2}C_D\rho A V_a^2$). Stars indicate the sum of the steady state drag F_{QS} and added mass force $m_v a$. Inset: peak drag force $\hat{F}_D$ as a function of acceleration. Open circles: measurements not included in main figure. Full line: fitted curve $\hat{F}_a \propto a^{0.5}$.

force $\hat{F}_D = F_D(t = t_a)$; the star symbols indicate the expected sum of the steady state force F_{QS} and the added mass force $m_v a$ [20]. Evidently, using the added mass for F_a strongly underestimates $\hat{F}_D$, and we would expect $\hat{F}_a \propto a^\kappa$ with $\kappa = 1$. However, the inset of Fig. 2, which presents the value $\hat{F}_D$ as a function of acceleration, shows that $\kappa = 0.51 \pm 0.05$. This value for κ was found from all possible combinations of 10 accelerations and 7 target velocities. A value of $\kappa < 1$ has been observed elsewhere [14,24], although there are no experimental data available over a substantial range of accelerations and velocities to assign a numerical value to κ.

Figure 3 shows the drag force F_D for an equal acceleration ($a = 1.23$ m/s^2) toward different target velocities. The dash-dotted lines show the force based on Eq. (1), including the added mass force for F_a. Again, we see a significant underestimation of the measured force, both during the acceleration as well as shortly thereafter. Furthermore, a virtual mass also cannot explain the gap between the measured force and predicted force after the acceleration phase has ended, since the added mass force would vanish instantaneously when the acceleration ceases. Similar to acceleration, we find $\hat{F}_a \propto V_a^\kappa$, with $\kappa = 0.52 \pm 0.04$ (Fig. 3, inset).

Hence, the empirical result $F_a \propto (aV)^{0.5}$ suggests the following scaling law:

$$F_a = C_a \times \rho A \sqrt{\nu a V}, \tag{3}$$

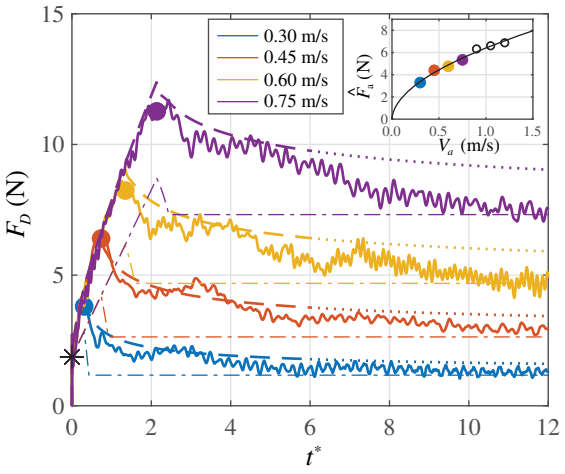

FIG. 3. Measured and predicted drag force for $a = 1.23$ m/s^2 toward different target velocities. Full lines indicate the measured force signals, full circles indicate the end of acceleration. The star ($*$) indicates the magnitude of added mass force $m_v a$ [20]; dash-dotted line: $\frac{1}{2} C_D \rho A V^2 + m_v a$; dashed then dotted line: $(\frac{1}{2} C_D \rho A V^2 + F_a)$, $t^* \leq 6$; dotted line: $(\frac{1}{2} C_D \rho A V^2 + F_a)$, $t^* > 6$. Inset: peak hydrodynamic force of the main figure as a function of V_a. Open circles: measurements not included in main figure. Full line: fitted curve $\hat{F}_a \propto V_a^{0.5}$.

where C_a is an instationary drag coefficient that depends on the plate geometry (similar to a conventional drag coefficient). This scaling follows from the ansatz below.

Equation (3) is directly found from the general solution for Stokes' first problem of the flow of a viscous fluid over a plate in a semi-infinite domain with an imposed velocity $V(t)$ [27,28]:

$$\begin{aligned} V(t) - u(y,t) &= \int_{-\infty}^{t} \frac{y}{\sqrt{4\pi\nu}} \frac{V(\tau)}{(t-\tau)^{3/2}} e^{-y^2/4\nu(t-\tau)} d\tau \\ &= at \left[\left(1 + \frac{y^2}{2\nu t}\right) \mathrm{erfc}\left(\frac{y}{2\sqrt{\nu t}}\right) \right. \\ &\quad \left. - \frac{y}{\sqrt{\pi\nu t}} \exp\left(-\frac{y^2}{4\nu t}\right) \right], \end{aligned} \tag{4}$$

for $V(t) = at$ when $0 < t \leq t_a$ [29], which includes the flow history, and describes the generation and diffusion of vorticity from the plate surface. The expression for $t > t_a$ is found by subtracting the right-hand side of Eq. (4) shifted by t_a over time from $u(y,t)$. The rate of momentum change per unit area, i.e., the shear force $F_a/A = \rho\nu \partial u/\partial y|_{y=0}$, for $V(t)$ as shown in Fig. 1(b) then gives:

$$F_a^{\mathrm{diff}}(t) = C \times \rho A a \sqrt{\nu} [\sqrt{t} - H(t - t_a)\sqrt{t - t_a}], \tag{5}$$

with $C = 2/\sqrt{\pi}$, and where $H(t)$ is the Heaviside step function. This expression gives Eq. (3) for $0 < t \leq t_a$, with $t = V/a$, but also gives asymptotically $F_a(t) \sim t^{-1/2}$ for $t \gg t_a$ when the acceleration ceases. The measurements (Fig. 1) show how vorticity is generated and advected into the vortex at the plate edge. This advection of momentum needs to be accounted for. We now generalize Eq. (5), where C_a represents the ratio of the advective momentum transfer over the diffusive momentum transfer; C_a can thus be interpreted as a "Nusselt number" for the momentum transfer, i.e., $C_a = F_a/F_a^{\mathrm{diff}}$ [30,31].

Figure 4(a) shows the measured hydrodynamic force $F_a(t^*)$ for different accelerations, corresponding to Fig. 2. We compare this to the modeled hydrodynamic force F_a from Eqs. (3)–(5) in Fig. 4(b), where we use $C_a = 291$ (see below) as the instationary drag coefficient. Note the close correspondence of the measured and predicted forces, both during the acceleration phase up to $t^* = t_a^*$, indicated by the circles, as well as during the relaxation phase ($t^* > t_a^*$) until the dash-dotted line at $t^* \cong 6$. This underlines the signature of $F_a(t)$ as a history force. Similarly to the measured hydrodynamic force, the lines in Fig. 4(b) collapse on a single curve $(t^*)^{-1/2}$ during the relaxation phase, indicated by the dashed line, which is the solution for an impulsively started plate [32].

The vorticity that is advected and fed into the vortex at the plate edges increases the circulation Γ of the vortex. This can be directly related to the drag force, i.e., $F_D(t)/\ell_b \propto \rho \dot{\Gamma} \ell_a$ [15,33,34], given that the vortex remains

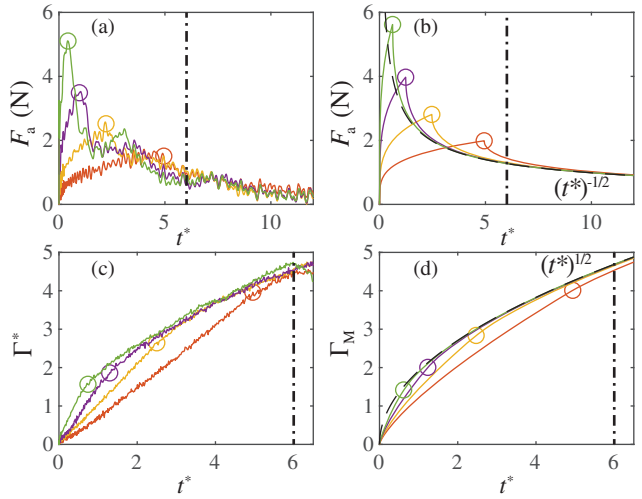

FIG. 4. Instationary drag force $F_a(t)$ and dimensionless circulation Γ^* [for region indicated in Fig. 1(h)]. Panels (a) and (c) are measurements; panels (b) and (d) follow from Eq. (5) with $C = C_a$. Colors correspond to the acceleration rates of Fig. 2; open circles indicate end of acceleration. Dashed line represents impulsively started case. Dash-dotted line at $t^* = 6$ marks the transition to a separated turbulent wake; cf. Fig. 1(h).

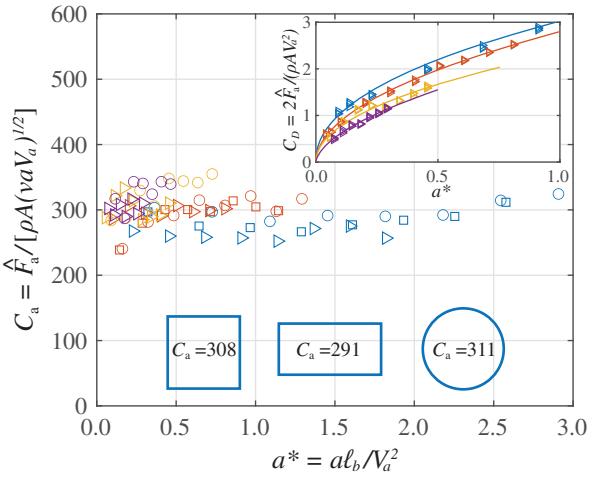

FIG. 5. Measured instationary drag coefficient C_a as a function of the dimensionless acceleration a^* for a circular disk ◯, and square □, and rectangular ▷ plates. Colors indicate different target velocities as in Fig. 3. Numbers in shapes represent mean values for C_a. Inset: drag coefficient $C_D = F_D/(\frac{1}{2}\rho AV_a^2)$ as a function of a^* during acceleration for the rectangular plate. Full lines: fitted curves $F_D \propto (a^*)^{0.5}$; colors indicate V_a as in Fig. 3.

attached to the plate edge. Figure 4(c) represents the measured circulation of the vortex at the plate edge as a function of dimensionless time for various rates of acceleration a. The dimensionless circulation Γ^* is computed as $\Gamma^* = \int_{S^*} \omega^* dS^*$, where $\omega^* = \omega \ell_b / V_a$ and $S^* = S/\ell_b^2$ is the integration area in the top half of our field of view, indicated in Fig. 1(h).

We compare this with modeled circulation Γ_M in Fig. 4(d), which is found from integrating the vorticity generated at the plate surface in Eq. (4): $\Gamma_M \propto \int_t (\partial u/\partial y)|_{y=0} dt$ [35]. The resemblance between the experiments and the model is striking, with Γ_M scaled to match Fig. 4(c). Note that the experimental data appear to diverge for $t^* > 6$. This coincides with the breakup of the initial vortex into smaller vortices, that subsequently develop into a three-dimensional separated turbulent wake behind the plate [36,37]. Both the measured and modeled circulations merge into a single curve for $t^* > t_a^*$. This curve, shown by the black dashed line, is the asymptote for an impulsively started plate that follows from Eq. (4) with $C = C_a$ for $t_a \to 0$ with constant $V_a = at_a$.

What remains is to present C_a as a function of a^* for various plate geometries. Figure 5 shows C_a that is found from the measured peak force $\hat{F}_a$ divided by $\rho A\sqrt{\nu a V_a}$, according to Eq. (3), for all imposed accelerations and all target velocities, for the circular disk and both square and rectangular plates. Nearly uniform values of C_a across all values of a^* and V_a are found, equal to $C_a = 291$ with a standard deviation of 20 for the rectangular plate, and slightly higher values for the square plate ($C_a = 308 \pm 36$) and circular disk ($C_a = 311 \pm 26$); see Fig. 5. These values do not appear to depend on either the magnitude of the acceleration or Reynolds number, but on plate geometry only. A variation of C_a with plate geometry is not unexpected, as stationary drag coefficients also differ slightly for plates with different shapes [38,39]. The inset of Fig. 5 shows the result for the scaling applied in previous studies [14,15] using $C_D = \hat{F}_a/(\frac{1}{2}\rho AV_a^2)$. It is clear that the data do not collapse on a single curve, but rather organize on different curves that follow $(a^*)^{0.5}$ for different target velocities V_a. Evidently, scaling with C_D [14,15] leaves a dependency on both a^* and V_a, which is resolved by using the scaling of Eq. (3) to obtain a uniform value for C_a.

Finally, we include in Fig. 3 the total drag force $F_D(t)$ from Eq. (1) with the history force $F_a(t)$ from Eqs. (3)–(5). The scaling in Eq. (3) now accurately predicts the drag force during the acceleration phase of the plate. After reaching the peak drag force (at t_a^*, indicated by the full circles in Fig. 3), the history force also describes the relaxation of the drag force, up to $t^* \cong 6$, where the vortex near the plate edges detaches and breaks up, and a turbulent wake is formed. After this we see a faster decay of the measured F_a, which is also seen in previous experiments [7] and could be similar to the decay of history forces on spherical particles at larger times [40]. An analytical expression for the history force exists for a sphere, which appears in the equation of motion for a small sphere in nonuniform flow at low Reynolds number (Re $\ll 1$) [41,42], but the contribution of the history force is often neglected or found to be insignificant compared to other forces [43–45]. The concept of noncirculatory and circulatory added mass [18,46] could provide a further

generalization to other accelerating objects. The present scaling for the generation of vorticity and transport into vortices that form near the object could provide a physical basis for vorticity estimations close to the object, when vorticity cannot be measured directly.

In summary, our experiments show that, contrary to what is generally accepted, the unsteady drag force is better described by a history force that scales as $F_a \propto \sqrt{a}$, rather than a noncirculatory added mass force (with $F_a \propto a$), for an accelerating normal plate at high Reynolds number. We conjecture that the added mass force becomes dominant for very large and short-duration accelerations ($a^* \gg 1$, $t_a^* \ll \frac{1}{2}$), i.e., where the velocity changes almost discontinuously [47]. The present Letter demonstrates the significance of the history force for plates with finite-duration accelerations.

This work is part of the "ImpulsiveFlows" project that has received funding from the European Research Council (ERC) under the EU Horizon 2020 program (Grant No. 884778).

*J.Reijtenbagh@tudelft.nl

[1] J. O. Dabiri, Annu. Rev. Fluid Mech. **41**, 17 (2009).
[2] D. Rival, T. Prangemeier, and C. Tropea, Exp. Fluids **46**, 823 (2009).
[3] G. D. Weymouth and M. S. Triantafyllou, J. Fluid Mech. **721**, 367 (2013).
[4] J. D. Eldredge and A. R. Jones, Annu. Rev. Fluid Mech. **51**, 75 (2019).
[5] P. Mancini, F. Manar, K. Granlund, M. V. Ol, and A. R. Jones, Phys. Fluids **27**, 123102 (2015).
[6] K. Mulleners, P. Mancini, and A. Jones, AIAA J. **55**, 2118 (2017).
[7] E. J. Grift, N. B. Vijayaragavan, M. J. Tummers, and J. Westerweel, J. Fluid Mech. **866**, 369 (2019).
[8] J. R. Morison, M. P. Obrien, J. W. Johnson, and S. A. Schaaf, J. Pet. Technol. **2**, 149 (1950).
[9] G. K. Batchelor, *An Introduction to Fluid Dynamics* (Cambridge University Press, Cambridge, England, 1967).
[10] C. E. Brennen, A review of added mass and fluid inertial forces, Technical Report, Naval Civil Engineering Laboratory, Sierra Madre, CA, 1982.
[11] G. Birkhoff, *Hydrodynamics* (Princeton University Press, Princeton, NJ, 1960).
[12] T. L. Daniel, American Zoologist **24**, 121 (1984).
[13] A. Leonard and A. Roshko, J. Fluids Struct. **15**, 415 (2001).
[14] J. N. Fernando, G. D. Weymouth, and D. E. Rival, J. Fluids Struct. **93**, 102835 (2020).
[15] Z. Li, Y. Xiang, S. Qin, H. Liu, and F. Wang, Phys. Fluids **34**, 081908 (2022).
[16] F. M. White, *Fluid Mechanics*, 7th ed. (McGraw-Hill, New York, 2011), pp. xv, 862.
[17] W. R. Graham, C. W. Pitt Ford, and H. Babinsky, J. Fluid Mech. **815**, 60 (2017).
[18] S. J. Corkery, H. Babinsky, and W. R. Graham, J. Fluid Mech. **870**, 492 (2019).
[19] G. Y. Dynnikova, Dokl. Phys. **64**, 397 (2019).
[20] P. R. Payne, Ocean Eng. **8**, 541 (1981).
[21] F. Odar and W. S. Hamilton, J. Fluid Mech. **18**, 302 (1964).
[22] T. Sarpkaya, AIAA J. **29**, 1283 (1991).
[23] M. Gharib, E. Rambod, and K. Shariff, J. Fluid Mech. **360**, 121 (1998).
[24] P. Koumoutsakos and D. Shiels, J. Fluid Mech. **328**, 177 (1996).
[25] G. Emanuel, *Analytical Fluid Dynamics*, 2nd ed. (CRC Press, Boca Raton, FL, 2000).
[26] See Supplemental Material at http://link.aps.org/supplemental/10.1103/PhysRevLett.130.174001 for a more detailed view of the velocity profile, drag force, circulation. and flow field over time.
[27] H. Schlichting and K. Gersten, *Boundary-Layer Theory*, 8th ed. (Springer, Berlin, 2000).
[28] C. T. Crowe, *Multiphase Flows with Droplets and Particles*, 2nd ed. (CRC Press, Boca Raton, FL, 2012).
[29] J. Crank, *The Mathematics of Diffusion*, 2nd ed. (Clarendon Press, Oxford, 1975).
[30] R. J. Goldstein, E. M. Sparrow, and D. C. Jones, Int. J. Heat Mass Transfer **16**, 1025 (1973).
[31] D. P. M. van Gils, S. G. Huisman, G.-W. Bruggert, C. Sun, and D. Lohse, Phys. Rev. Lett. **106**, 024502 (2011).
[32] C. J. Wang and J. D. Eldredge, Theor. Comput. Fluid Dyn. **27**, 577 (2013).
[33] H. Lamb, *Hydrodynamics* (Cambridge University Press, Cambridge, England, 1916).
[34] S. J. Corkery, R. J. Stevens, and H. Babinsky, Low Reynolds number surge response of a flat plate wing at 90 degrees incidence, in *Proceedings of the 55th AIAA Aerospace Sciences Meeting* (2017).
[35] J. C. Wu, AIAA J. **19**, 432 (1981).
[36] M. J. Ringuette, M. Milano, and M. Gharib, J. Fluid Mech. **581**, 453 (2007).
[37] J. N. Fernando and D. E. Rival, J. Fluid Mech. **799**, R3 (2016).
[38] S. F. Hoerner, *Fluid-Dynamic Drag* (Hoerner Fluid Dynamics, Bakersfield, CA, 1965).
[39] R. D. Blevins, *Applied Fluid Dynamics Handbook* (Krieger Publishing, Malabar, 2003).
[40] R. W. Mei and R. J. Adrian, J. Fluid Mech. **237**, 323 (1992).
[41] M. R. Maxey and J. J. Riley, Phys. Fluids **26**, 883 (1983).
[42] R. Mei, C. J. Lawrence, and R. J. Adrian, J. Fluid Mech. **233**, 613 (1991).
[43] A. T. Hjelmfelt and L. F. Mockros, Appl. Sci. Res. **16**, 149 (1966).
[44] K. Hishida and Y. Sato, Multiphase science and technology **10**, 323 (1998).
[45] P. Bagchi and S. Balachandar, Phys. Fluids **15**, 3496 (2003).
[46] P. Gehlert and H. Babinsky, J. Fluid Mech. **915**, A50 (2021).
[47] T. von Kármán, The impact on seaplane floats during landing, Technical Report, 321 NACA, Washington, DC, 1929.